nature nanotechnology

SUPPLEMENTARY INFORMATION

https://doi.org/10.1038/s41565-018-0282-0

In the format provided by the authors and unedited.

Spin–orbit torque driven by a planar Hall current

Christopher Safranski[1,2], Eric A. Montoya[1,2] and Ilya N. Krivorotov[1*]

[1]Department of Physics and Astronomy, University of California, Irvine, CA, USA. [2]These authors contributed equally: Christopher Safranski, Eric A. Montoya. *e-mail: ilya.krivorotov@uci.edu

Supplementary Material for Spin-orbit torque driven by a planar Hall current

Chris Safranski, Eric A. Montoya, Ilya N. Krivorotov

Supplementary Note 1: Multilayer deposition

The multilayers are deposited by magnetron sputtering on Al_2O_3 (0001) substrates in 2 mTorr Ar with a base pressure $\leq 3.0 \times 10^{-8}$ Torr. The film stacks consist of ferromagnetic metal (FM) and non-magnetic metal (NM) layers and have the following structure types:

1. Al_2O_3 (0001)/NM_1/FM/Ta(4 nm)
2. Al_2O_3 (0001)/Ta(3 nm)/Au(2.5 nm)/FM/Au(1.5 nm)/Ta(4 nm)
3. Al_2O_3 (0001)/Ta(3 nm)/Au(3.9 nm)/FM/Au(1 nm)/AlO_x(2 nm)

For all samples, a 3 nm Ta seed layer is employed to promote growth of a smooth multilayer [1] and the Ta or AlO_x capping layer prevents the multilayer oxidation. Here, AlO_x(2 nm) is a 2 nm layer of Al that is allowed to naturally oxidise. The composite FM layer is a superlattice of exchange coupled Co and Ni layers: Co(0.85 nm)/Ni(1.28 nm)/Co(0.85 nm)/Ni(1.28 nm)/Co(0.85 nm). We have chosen the Co/Ni superlattice due to its large planar Hall effect (PHE) and anisotropic magnetoresistance (AMR) [2] as well as its significant perpendicular magnetic anisotropy (PMA) [3, 4]. The thicknesses of the Co and Ni layers in the composite FM are chosen to nearly balance the easy plane magnetic shape anisotropy of the FM film by PMA in order to be able to saturate the FM magnetization in any direction by a small magnetic field. In type 1 multilayers, we use NM_1 = Ta(3 nm)/Pt(7.0 nm), Ta(3 nm)/Pd(8.0 nm), or Ta(3 nm)/Au(3.9 nm), with the Au, Pd, and Pt thickness chosen to keep the NM_1 layer sheet resistance nearly the same. Type 1 samples allow us to explore effects due the bottom NM_1 and NM_1/FM interface. Type 2 and 3 multilayers allow us to explore the role of the top FM/NM_2 interface in comparison to type 1 multilayers. The thin top Au layers in type 2 and 3 multilayers are known to form continuous film due to the excellent wetting of Co by Au [5, 6]. For type 2 multilayer, the thickness of the top and bottom Au layers are chosen to be different in order to generate a non-zero microwave Oersted field applied to the FM magnetization in ST-FMR measurements, which strongly enhances the amplitude of the magnetic oscillations and the signal-to-noise ratio of the ST-FMR signal. For type 3 multilayer, we use the bottom NM_1 = Ta(3 nm)/Au(3.9 nm), as in type 1, but replace the Ta cap by Au/AlO_x.

Supplementary Note 2: Sheet resistance measurements

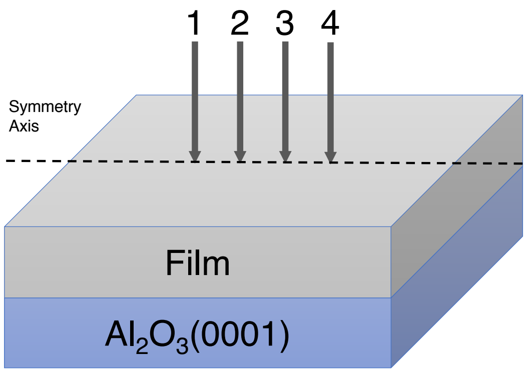

Supplementary Figure 1: Schematic of 4-point probe measurement.

We make sheet resistance measurements of magnetic multilayers by the collinear four point probe technique [7]. Four equidistant probes make contact along the symmetry axis of film samples, as shown in Supplementary Fig. 1. The resistances $R_A = V_{23}/I_{14}$, $R_B = V_{24}/I_{13}$, and $R_C = V_{43}/I_{12}$ are measured by means of 4 terminal source-meter.

The subscripts on I and V indicate the probes where current is supplied and voltage is measured; for example, for R_A, a direct current I is supplied between points 1 and 4 and the voltage is measured at points 2 and 3. R_A, R_B, and R_C must satisfy the following two relations [8]:

$$\exp\left(-\frac{2\pi R_A}{R_\mathrm{S}}\right) + \exp\left(-\frac{2\pi R_C}{R_\mathrm{S}}\right) = 1 \tag{S1}$$

and

$$\exp\left(\frac{2\pi R_A}{R_\mathrm{S}}\right) - \exp\left(\frac{2\pi R_B}{R_\mathrm{S}}\right) = 1, \tag{S2}$$

where R_S is the sheet resistance of the film. Small deviations in probe spacing are corrected by averaging a symmetric measurement for the Rs, and thermal voltages/offsets are accounted for by switching voltage leads, therefore:

$$\begin{aligned} R_A &= \left(V_{23}/I_{14} + |V_{32}|/I_{14}\right)/2 \\ R_B &= \left(V_{24}/I_{13} + V_{13}/I_{24} + |V_{42}|/I_{13} + |V_{31}|/I_{24}\right)/4 \\ R_C &= \left(V_{43}/I_{12} + V_{12}/I_{43} + |V_{34}|/I_{12} + |V_{21}|/I_{43}\right)/4. \end{aligned} \tag{S3}$$

The measured sheet resistances of various multilayer films are summarized in Supplementary Table I. The current densities in each layer can be determined from the parallel resistor model. The top Ta(4 nm) is taken to have the same resistivity as the bottom Ta(3 nm) because approximately 1 nm of the top Ta layer oxidises under ambient conditions [9]. The data in Table I demonstrate that the Ta layers have much higher sheet resistances than other layers in the multilayer stack and thus the electric current density in the Ta layers is small in all our measurements.

Supplementary Table I: Summary of film level sheet resistances determined by 4 point probe measurements. Numbers in parenthesis are layer thickness in nm. All measurements are performed at room temperature unless indicated otherwise.

Sample	R_S (Ω)
Ta(3.0)	929
Ta(3.0)/Au(3.9)	27.0
Ta(3.0)/Au(3.9) [77 K]	24.5
Ta(3.0)/Pt(7.0)	28.2
Ta(3.0)/Pd(8.0)	27.9
Ta(3.0)/Au(3.9)/[Co(0.85)/Ni(1.28)]$_2$/Co(0.85)/Ta(4.0)	19.3
Ta(3.0)/Au(3.9)/[Co(0.85)/Ni(1.28)]$_2$/Co(0.85)/Ta(4.0) [77 K]	15.4
Ta(3.0)/Pt(7.0)/[Co(0.85)/Ni(1.28)]$_2$/Co(0.85)/Ta(4.0)	20.5
Ta(3.0)/Pd(8.0)/[Co(0.85)/Ni(1.28)]$_2$/Co(0.85)/Ta(4.0)	17.3
Ta(3.0)/Au(2.5)/[Co(0.85)/Ni(1.28)]$_2$/Co(0.85)/Au(1.5)/Ta(4.0)	22.2

Supplementary Note 3: Spin torque ferromagnetic resonance

We measure the ferromagnetic resonance linewidth as a function of direct current bias in the nanowire devices by spin-torque ferromagnetic resonance (ST-FMR) [10–12]. In this method, a rectified voltage V_mix generated by the sample in response to the applied microwave current is measured as a function of the drive frequency and external magnetic field [13]. Resonances in V_mix are observed at the frequency and field values corresponding to spin wave eigenmodes of the system [14]. To improve the sensitivity of the method, we modulate the applied magnetic field and use lock-in detection to measure ac voltage $\tilde{V}_\mathrm{mix}$ generated by the sample at the frequency of the magnetic field modulation as illustrated in Supplementary Fig. 2 [15]. This signal is proportional to magnetic field derivative of the rectified voltage $\tilde{V}_\mathrm{mix}(H) \sim dV_\mathrm{mix}(H)/dH$.

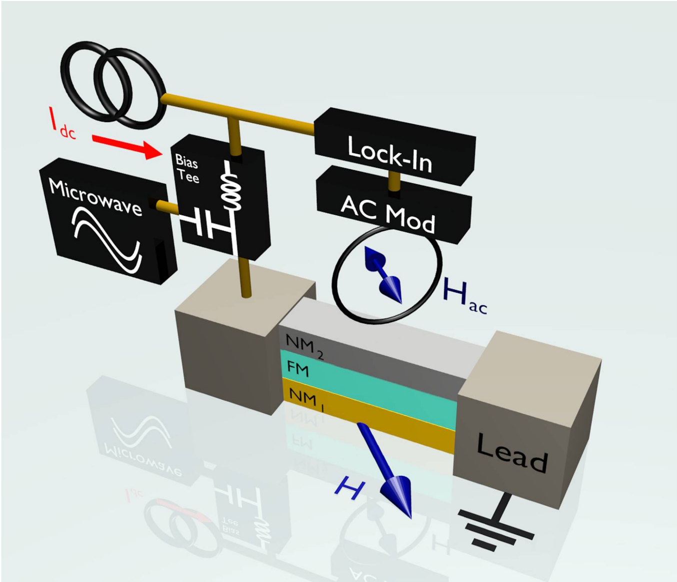

Supplementary Figure 2: Schematic of the setup for ST-FMR measurements with magnetic field modulation.

Supplementary Note 4: Generated microwave power and the critical current

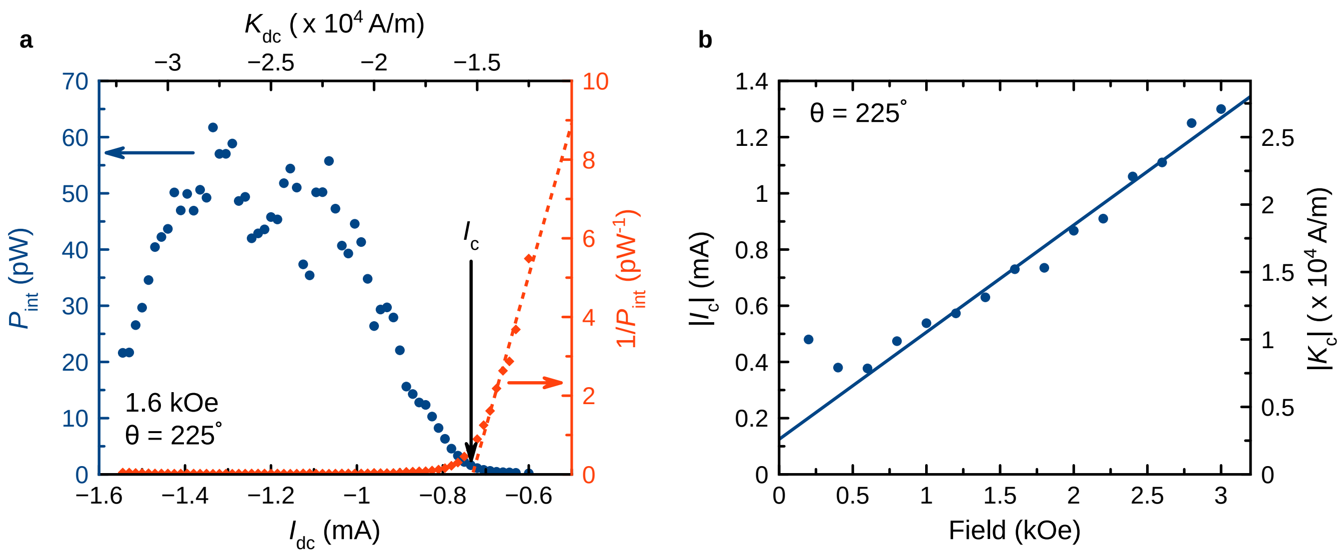

Supplementary Figure 3: **The microwave emission properties of the Ta(3 nm)/Au(3.9 nm)/FM/Ta(4 nm) nanowire device. a**, Integrated power P_{int} emitted by the lowest frequency spin wave mode M_1 at $T = 77\,\mathrm{K}$ (blue symbols) as a function of current bias measured in a 1.6 kOe magnetic field applied at $\theta = 225°$. The inverse power $1/P_{\mathrm{int}}$ is shown by red symbols. **b**, Absolute value of the critical current for the onset of the auto-oscillations $|I_c|$ as a function of magnetic field applied at $\theta = 225°$.

When direct current I_{dc} applied to the nanowire spin torque nano-oscillator (STNO) exceeds a critical value I_c, the magnetization of the FM layer enters an auto-oscillatory state, which gives rise to microwave power generation by the STNO device. We find that several spin wave eigenmodes of the nanowire enter the auto-oscillatory state, however most of the microwave power is generated by auto-oscillations of the lowest-frequency spin wave mode M_1. The integrated power P_{int} (blue symbols) emitted by mode M_1 in the Ta(3 nm)/Au(3.9 nm)/FM/Ta(4 nm) nanowire device is shown in Supplementary Fig. 3a. Here the power delivered to a 50 Ω load and corrected for frequency dependent attenuation and amplification in the microwave measurement circuit is given [16]. The data in Supplementary Fig. 3a are collected at $T = 77\,\mathrm{K}$ in a $1.6\,\mathrm{kOe}$ magnetic field applied at $\theta = 225^\circ$ in the xz plane. We observe a large increase in the emitted microwave power above the background level for $I_{\mathrm{dc}} < -0.7\,\mathrm{mA}$. A more precise evaluation of I_{c} can be obtained by fitting the inverse of the integrated power (red symbols in Supplementary Fig. 3a) to a straight line for sub-critical values of I_{dc} [17]. The critical current obtained via such a procedure from the data in Supplementary Fig. 3a is $I_{\mathrm{c}} = -0.73\,\mathrm{mA}$.

Supplementary Figure 3b shows the dependence of I_{c} on magnetic field H applied at $\theta = 225^\circ$ in the xz plane. Apart from the low field regime, this dependence is well fit by a straight line. This linear dependence of I_{c} on H is expected for our devices because magnetic anisotropy of the nanowire is relatively small [17, 18]. In the low field regime, magnetization of the nanowire starts to deviate from the applied field direction that maximizes the PHT efficiency ($\theta = 225^\circ$), which leads to an increase of I_{c}.

The microwave power emitted by this STNO in the M_1 mode is approximately $60\,\mathrm{pW}$ at $I_{\mathrm{dc}} = -1.3\,\mathrm{mA}$, which significantly exceeds the output power of spin Hall STNOs measured at higher currents [19]. The reason for the improved efficiency of PHT STNO is the angular dependence of AMR, which maximizes the amplitude of resistance oscillations for magnetization making a 45° angle with respect to the electric current direction. This magnetization direction in the xz plane is also the direction of maximum efficiency of the PHT. This is to be contrasted with SHT STNOs, for which the direction of maximum negative damping efficiency ($\hat{\mathbf{y}}$) minimizes the amplitude of AMR oscillations.

Supplementary Note 5: Comparison to Rashba SOT models

Rashba SOC at a FM/NM interface can give rise to field-like and damping-like SOTs. Therefore, it is important to understand if the biaxial antidamping torque reported in this manuscript can be of Rashba origin. Rashba torque at the interface between FM and NM metals originates from an electric field perpendicular to the interface that arises from inversion symmetry breaking at the interface. In the presence of a non-zero SOC at the interface, such an electric field gives rise to an interfacial SOT [20]. The Rashba interaction is strongly localized to the vicinity of the FM/NM interface due to very efficient electric field screening in metals. Calculations show that the Rashba SOT for the FM and NM materials considered here is localized to a few atomic layers at the FM/NM interface [21, 22]. The magnitude of the Rashba SOT is determined by a material-specific interfacial Rashba coupling constant α_{R} that increases with increasing interfacial electric field and interfacial SOC coupling [20].

The dependence of the Rashba SOT on the direction of magnetization $\hat{\mathbf{m}}(\theta,\phi)$ can be a function of many parameters such as α_{R}, exchange coupling in the FM [23–25] and anisotropy of spin relaxation induced by Rashba SOT [26]. Quite complex angular dependences of the Rashba SOT were predicted in various theoretical models of this effect [23–26]. Here we review some of the angular dependences of Rashba SOTs and compare them to our data. For easy comparison to ST-FMR data, SOTs can be decomposed into conservative and non-conservative components. The non-conservative components can dynamically add or remove magnetic energy to the system and thus can act as damping and antidamping (and thus modulate ST-FMR linewidth). The conservative components can modify the magnetic energy landscape (and thus modulate ST-FMR resonance frequency). Here we concentrate on evaluation of the non-conservative components of Rashba SOTs. The angular dependence of a current-induced effective magnetic damping $\alpha_{\mathrm{st}}(\theta,\phi)$ arising from a SOT vector $\vec{\tau}_{\mathrm{st}}(\theta,\phi)$ is proportional to divergence of the SOT vector on the unit sphere [27]: $\vec{\nabla}_{\theta,\phi}\cdot\vec{\tau}_{\mathrm{st}}(\theta,\phi) = \frac{1}{\sin(\theta)}\left[\frac{\partial(\sin(\theta)\tau_\theta)}{\partial\theta} + \frac{\partial\tau_\phi}{\partial\phi}\right]$, where (τ_θ,τ_ϕ) are the components of $\vec{\tau}_{\mathrm{st}}(\theta,\phi)$ in spherical coordinates. Therefore, $\alpha_{\mathrm{st}}(\theta,\phi) \sim \vec{\nabla}_{\theta,\phi}\cdot\vec{\tau}_{\mathrm{st}}(\theta,\phi)$ is a convenient quantity for characterization of the angular dependence of the non-conservative component of a SOT and for direct comparison to the measured angular dependence of the current-induced variation of the ST-FMR linewidth $d\Delta H/dK_{\mathrm{dc}}(\theta,\phi)$.

Kurebayashi et al. [24] considered the limit in which Rashba coupling is much weaker than the FM exchange. In this limit, the interplay between the Rashba coupling and exchange interaction results in a current-driven effective Rashba field $\vec{H}_{\mathrm{R}} \sim \cos(\theta_{\mathrm{M-E}})\hat{\mathbf{z}} = \sin(\theta)\cos(\phi)\hat{\mathbf{z}}$ in the film normal direction ($\hat{\mathbf{z}}$), where $\theta_{\mathrm{M-E}}$ is the angle between magnetization ($\hat{\mathbf{m}}$) and the applied electric field ($\hat{\mathbf{x}}$). In this case, the SOT is $\vec{\tau}_{\mathrm{st}} \sim \hat{\mathbf{m}}\times\vec{H}_{\mathrm{R}}$, and evaluation of the divergence of this SOT gives: $\alpha_{\mathrm{st}}(\theta,\phi) \sim \vec{\nabla}_{\theta,\phi}\cdot\vec{\tau}_{\mathrm{st}}(\theta,\phi) \sim \sin(\theta)\sin(\phi)$. This uniaxial angular dependence of the antidamping SOT is identical to that of SHT shown in Fig. 3f of the main text. Therefore, the observed biaxial antidamping SOT cannot be explained by the model of Kurebayashi et al.

When Rashba SOC and FM exchange interaction become of comparable magnitude, the Rashba SOT can acquire a more complicated angular dependence [23, 25, 26]. In this case, the Rashba SOT can be expressed as a sum of several terms with different angular symmetries. In a Rashba model taking account of anisotropic spin relaxation [26], one term in the Rashba SOT expansion gives rise to a 180°-periodic antidamping SOT in the xz plane. This SOT term $\vec{\tau}_{\rm st} \sim \cos(\theta_{\rm M-E})\hat{\mathbf{m}} \times (\hat{\mathbf{z}} \times \hat{\mathbf{m}})$ results in the angular dependence of current-driven damping $\alpha_{\rm st}(\theta,\phi) \sim \vec{\nabla}_{\theta,\phi} \cdot \vec{\tau}_{\rm st}(\theta,\phi) \sim \cos(\theta)\sin(\theta)\cos(\phi)$, which has the same biaxial symmetry as that observed for the samples studied in this work.

Although one term in the Rashba SOT expansion can reproduce the angular dependence of the observed biaxial antidamping torque, a number of experimental observations are inconsistent with the Rashba origin of this torque:

- **The magnitude of PHT is not correlated with $\alpha_{\mathbf{R}}$.** The Rashba coupling constant α_R at the Co/Pt interface ($\alpha_{\rm R}^{\rm Pt} \approx 0.10\,{\rm eV\,nm}$) [28, 29] exceeds that at the Co/Pd and Co/Au interfaces ($\alpha_{\rm R}^{\rm Au} \approx \alpha_{\rm R}^{\rm Pd} \approx 0.03\,{\rm eV\,nm}$) [30, 31] by approximately a factor of three, which is inconsistent with similar values of the torque magnitude measured for these three interfaces (see Fig. 3b of the main text).

- **The Rashba model that can provide the antidamping torque with PHT symmetry in the xz plane, necessarily implies an antidamping torque in the xy plane.** The Rashba models with exchange [20, 23, 24, 26] predict an antidamping SOT term with symmetry identical to that of SHT ($\vec{\tau}_{\rm st} \sim (\hat{\mathbf{m}} \times (\hat{\mathbf{y}} \times \hat{\mathbf{m}}))$ and magnitude proportional to α_R. In such models, a non-zero biaxial antidamping SOT in the xz plane implies the presence of a non-zero antidamping torque with the SHT symmetry, which is inconsistent with the data for the Ta(3 nm)/Au(3.9 nm)/FM/Ta(4 nm) sample shown in Fig. 3a and Fig. 3b of the main text.

- **Under Rashba model, samples with identical NM/FM and FM/NM interfaces should exhibit similar torques.** Rashba SOC does not explain large differences in the SOT magnitude observed for samples with identical FM/NM interfaces such as Ta(3 nm)/Au(2.5 nm)/FM/Au(1.5 nm)/Ta(4 nm) and Ta(3 nm)/Au(3.9 nm)/FM/Au(1 nm)/AlO$_x$(2 nm). The data in Supplementary Note 6 show that the biaxial antidamping SOT in the xz plane of the Ta(3 nm)/Au(3.9 nm)/FM/Au(1 nm)/AlO$_x$(2 nm) sample is as strong as that measured in the Ta(3 nm)/Au(3.9 nm)/FM/Ta(4 nm) sample, while this torque is zero in the Ta(3 nm)/Au(2.5 nm)/FM/Au(1.5 nm)/Ta(4 nm) sample (see Fig. 1g of the main text). Given the screening length in Au is well below the Au layer thickness in our samples, Rashba SOTs arising from electric field at the FM/Au interface [20] are expected to be nearly independent of the cap layer material (Ta versus AlO$_x$). In contrast, the above samples show the magnitude of PHT depends strongly on NM layers that are not in direct contact with the FM layer.

- **Rashba torque is expected to generate large field-like components.** Such large field-like components would result in ST-FMR resonance frequency line shifts that are linear in current [32]. The ST-FMR data in Supplementary Figure 4 reveal that ST-FMR resonance frequency shifts are nearly quadratic in current (as expected from ohmic heating) with negligible components linear in current.

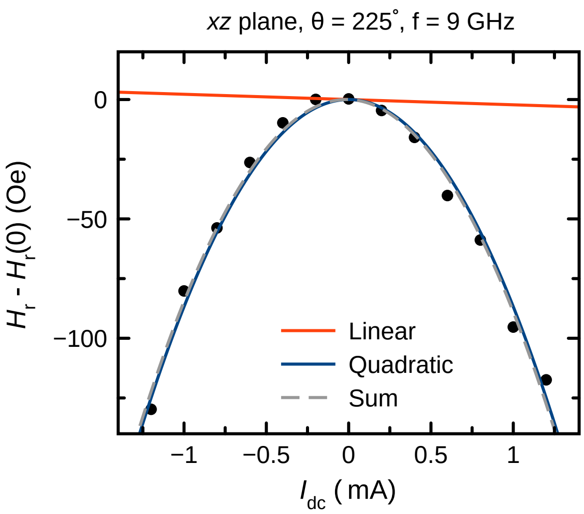

Supplementary Figure 4: The shift of the resonance field $H_{\rm r}$ from the resonance field with no applied current $H_{\rm r}(0)$ as a function of bias.

Supplementary Note 6: Effect of NM layers on PHT

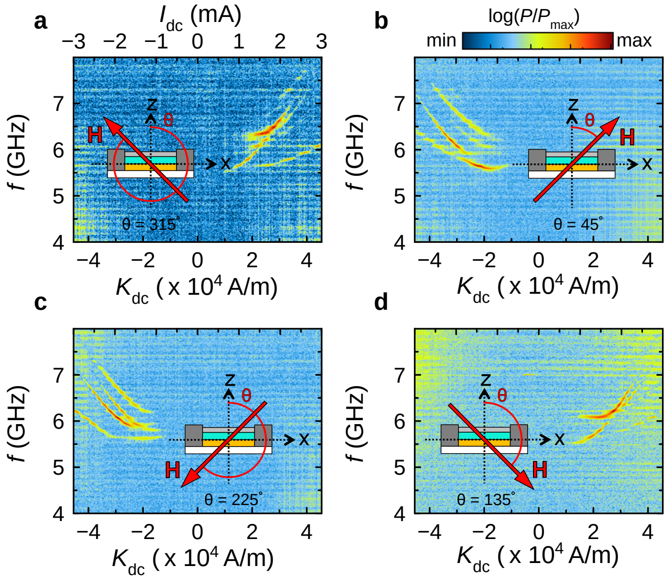

Supplementary Figure 5: **Microwave generation at T = 77 K.** Normalized power spectral density of microwave signal generated by the Ta/Au/FM/Au/AlO_x device in a 1.7 kOe magnetic field applied in the xz plane at four angles **a**, $\theta = 315°$, **b**, $\theta = 45°$, **c**, $\theta = 225°$, and **d**, $\theta = 135°$.

The majority of samples studied in this work are capped with a 4 nm thick Ta layer. In order to examine the role of the FM/Ta interface in generation of the biaxial antidamping SOT, we replace the Ta(4 nm) cap with a Au(1 nm)/AlO_x(2 nm) bilayer. Our measurements reveal that the biaxial antidamping SOT in the Ta(3 nm)/Au(3.9 nm)/FM/Au(1 nm)/AlO_x(2 nm) nanowire device is as strong as that in the Ta(3 nm)/Au(3.9 nm)/FM/Ta(4 nm) device, which reveals that SOC at the FM/Ta interface is not the origin of the observed torque.

Supplementary Fig. 5 shows our measurements of the microwave signal generation by the Ta(3 nm)/Au(3.9 nm)/FM/Au(1 nm)/AlO_x(2 nm) nanowire device at $T = 77$ K as a function of magnetic field angle in the xz plane and direct current density. The angular symmetry of the antidamping torque in this device is identical to that of the Ta(3 nm)/Au(3.9 nm)/FM/Ta(4 nm) device shown in Fig. 2 of the main text. Furthermore, the sheet critical current density K_c for excitation of auto-oscillatory dynamics is approximately equal for both devices, which demonstrates that the torque magnitude in these devices is nearly the same.

It is instructive to compare the enhancement of damping induced by spin pumping (Supplementary Note 7) to the magnitude of PHT for samples with different NM layers. As shown in Supplementary Note 7, damping enhancement due to spin pumping in the Ta/FM/Ta sample is small and thus Ta does not behave as a good spin sink in direct contact with Co in our samples. Changes in the top and bottom NM layer materials modify the damping due to spin pumping and the PHT magnitude in a systematic manner:

1. **Ta/Au/FM/Ta:** Insertion of the Au layer on the bottom, significantly increases the damping demonstrating efficient spin transfer across the Au/FM interface and efficient spin sinking in the Ta/Au layer. This sample with one efficient spin sink (bottom) showed large PHT, consistent with the transfer of planar Hall spin current only at one interface.

2. **Ta/Au/FM/Au/Ta:** With an additional Au insertion layer at the top, the damping increases further showing that this sample has two effective spin sinks of Ta/Au (bottom) and Au/Ta (top). This sample displays negligible PHT, which is consistent with the model of the transfer of planar Hall spin currents at the two interfaces cancelling out.

3. **Ta/Au/FM/Au/AlO_x:** Replacing the top Ta layer of Ta/Au/FM/Ta with Au/AlO_x leads to a similar damping as the Ta/Au/FM/Ta (bottom sink) sample and a reduction in damping compared to the Ta/Au/FM/Au/Ta (bottom and top sink) sample. This shows that the top Au/AlO_x layer does not behave as an efficient spin sink.

This sample once again shows large PHT, consistent with the net transfer of planar Hall spin current only at one interface (bottom).

These dependences of spin pumping and PHT on the NM layer materials further confirm that PHT cannot be attributed to SOC at the FM/Ta interface. Furthermore, comparing samples 2 and 3 above, PHT cannot be attributed purely to the FM/NM interfaces as both samples have Au/FM/Au structure. Our data show that one of the NM layers in a NM/FM/NM multilayer must be a good spin sink (reservoir) while the other layer must be a poor spin sink (reservoir) in order to generate large PHT. A corollary is that the planar Hall current in a standalone FM conductor cannot give rise to an antidamping SOT. A net transfer of angular momentum by the planar Hall current between the FM layer and the adjacent NM layers is required for generation of an antidamping SOT by the planar Hall current.

Supplementary Note 7: Broadband ferromagnetic resonance

We employ a conventional broadband ferromagnetic resonance technique (FMR) to measure magnetic damping in the $NM_1/FM/NM_2$ multilayer films in order to characterize spin pumping across the NM/FM interfaces and spin sink efficiencies of the NM layers. FMR measurements are carried out at room temperature using a broadband microwave generator, coplanar wave guide, and planar-doped detector diode. The measurements are performed at discrete frequencies in an in-plane field-swept, field-modulated configuration, as detailed in Ref. [33]. The measured FMR data are described by an admixture of the $\chi^{'}$ and $\chi^{''}$ components of the complex transverse magnetic susceptibility, $\chi = \chi^{'} + i\chi^{''}$. The FMR data are fit as described by Ref. [33, 34].

The Landau-Lifshitz-Gilbert (LLG) equation describes the magnetization dynamics in the FMR experiment:

$$\frac{\partial \mathbf{M}}{\partial t} = -\gamma \left[\mathbf{M} \times \mathbf{H}_{\mathrm{eff}}\right] + \alpha \left[\mathbf{M} \times \frac{\partial \hat{\mathbf{m}}}{\partial t}\right], \tag{S4}$$

where $\mathbf{M}$ is the instantaneous magnetization vector with magnitude M_{s}, $\hat{\mathbf{m}}$ is the unit vector parallel to $\mathbf{M}$, $\mathbf{H}_{\mathrm{eff}}$ is the sum of internal and external magnetic fields, $\gamma = g\mu_{\mathrm{B}}/\hbar$ is the absolute value of the gyromagnetic ratio, g is the Landé g-factor, μ_{B} is the Bohr magneton, $\hbar$ is the reduced Planck constant, and α is the dimensionless Gilbert damping parameter.

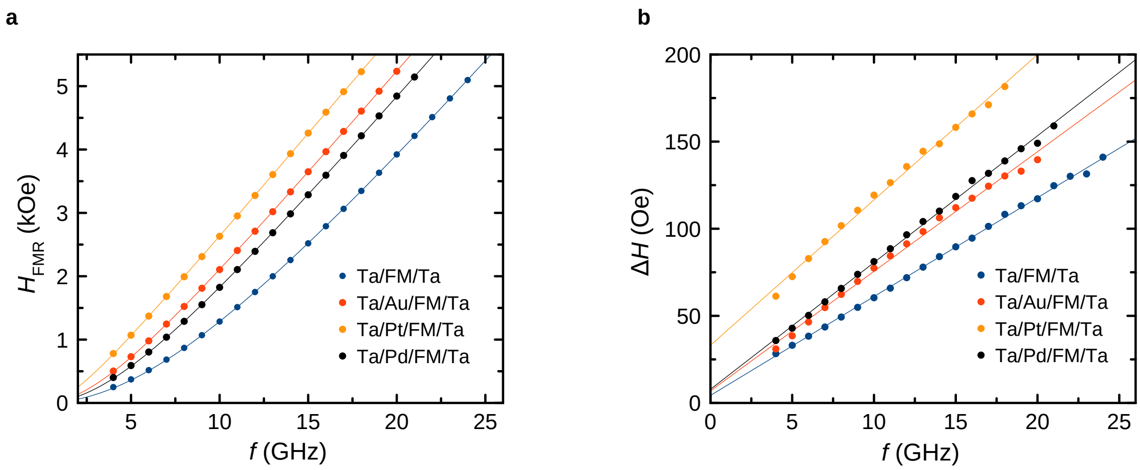

Supplementary Figure 6: **Broadband ferromagnetic resonance measurements performed on the film level.** **a**, Resonance field as a function of frequency f measured in the in-plane magnetic field configuration. **b**, FMR linewidth ΔH as a function of frequency.

The samples studied are polycrystalline and show negligible in-plane anisotropy. The in-plane resonance condition is

$$\left(\frac{\omega}{\gamma}\right)^2 = \left(H_{\mathrm{FMR}}\right)\left(H_{\mathrm{FMR}} + 4\pi M_{\mathrm{eff}}\right), \tag{S5}$$

Supplementary Table II: Summary of film level magnetic properties determined by broadband ferromagnetic resonance. Numbers in parenthesis are layer thickness in nm. The composite ferromagnet is FM=$[Co(0.85)/Ni(1.28)]_2/Co(0.85)$.

Sample	$4\pi M_{\rm eff}$ (Oe)	g	α (10^{-3})	$\Delta H(0)$ (Oe)
Ta(3.0)/FM/Ta(4.0)	7160	2.17	17.2	4
Ta(3.0)/Au(3.9)/FM/Ta(4.0)	3010	2.17	20.9	7
Ta(3.0)/Au(2.5)/FM/Au(1.5)/Ta(4.0)	3220	2.14	21.7	4
Ta(3.0)/Pt(7.0)/FM/Ta(4.0)	1480	2.17	25.3	33
Ta(3.0)/Pd(8.0)/FM/Ta(4.0)	4060	2.18	22.2	8
Ta(3.0)/Au(3.9)/FM/Au(1.0)/AlO_x(2.0)	2760	2.14	20.6	20

where $\omega = 2\pi f$ is the microwave angular frequency, $H_{\rm FMR}$ is the resonance field, $4\pi M_{\rm eff} = 4\pi M_{\rm s} - 2K_{\rm U}/M_{\rm s}$, and $K_{\rm U}$ is the perpendicular-to-film-plane uniaxial anisotropy. Supplementary Figure 6a shows example data of $H_{\rm FMR}$ as a function of frequency. The data are fit using equation S5 to extract $4\pi M_{\rm eff}$ and g, which are tabulated in Supplementary Table II.

The measured FMR linewidth defined as half-width of the resonance curve is well described by Gilbert-like damping,

$$\Delta H(\omega) = \alpha\frac{\omega}{\gamma} + \Delta H(0), \tag{S6}$$

where $\Delta H(0)$ is the zero-frequency line broadening due to long range magnetic inhomogeneity [35–37]. Supplementary Figure 6b shows example data of ΔH as a function of frequency. The data are fit using equation S6 to extract the parameters α and $\Delta H(0)$, which are tabulated in Supplementary Table II.

We use the values of α as a probe of efficiency of spin transfer across the FM/NM interface. When the spin transfer is efficient, an increase of the damping due to the spin pumping mechanism is expected [38–40]. The values of α in Supplementary Table II show that the Ta/FM/Ta sample has the lowest damping. This means that the spin pumping is smallest at the Ta/FM and FM/Ta interfaces. These data imply that spin current density across the FM/Ta interface is low and thus PHT arising from net spin current across this interface is small. Adding a Au insertion layer at the bottom Ta/FM interface, Ta/FM/Ta $\rightarrow$ Ta/Au/FM/Ta, shows a significant increase in the spin pumping induced damping. It is noteworthy that the thickness of Au(3.9 nm) is much less than the spin diffusion in Au (30-60 nm) suggesting that the Au/Ta bilayer acts as an efficient spin sink. Furthermore, adding another Au layer between the top FM/Ta interface shows further increase in spin pumping induced damping. This shows that the Au layer in the Au/Ta bilayer facilitates efficient spin transfer from the FM layer. The values of α in the Ta/Pt/FM/Ta and Ta/Pd/FM/Ta structures are high, indicating that the Pt and Pd layers are efficient spin current sinks in agreement with literature [41, 42]. Furthermore, some of the additional damping at the Pd and Pt interfaces can be due to proximity induced damping [43, 44], which is distinctly different from spin pumping induced spin transfer [40].

The result of low damping at the FM/Ta interface is somewhat surprising as much literature has shown that many FM/Ta exhibit significant spin pumping induced damping [9, 45], i.e. Ta acts as an efficient spin sink when adjacent to a FM. However, there are other cases where spin pumping directly into Ta does not occur. In one of the earliest spin pumping experiments on NM/NiFe/NM films, Mizukami et. al. [41] showed large interface damping when NM = Pt, Pd, but no interface damping when NM = Ta. A similar effect was seen by Liu et. al. [46] at the Ta/CoFeB interface. More recently, Singh et. al. [47], have shown spin pumping experiments in Ta/NM_A/Co/NM_B/Ta, Ta/Co/Ta, and Cu/Ta/Cu samples, where NM_A and NM_B are various combinations of Pt and Au layers. Their results are consistent with our data in Supplementary Table II and show, that under certain sample growth conditions, spin transfer from Co to Ta at the Co/Ta interfaces is inefficient.

We additionally grow a control sample to show that PHT does not originate from the top FM/Ta interface. In this sample, we replace the Ta cap with a Au(1.0 nm)/AlO_x(2.0 nm) bilayer, Ta/Au/FM/Ta $\rightarrow$ Ta/Au/FM/Au/AlO_x. This Au/AlO_x capped sample has a similar damping to the Ta capped sample (Supplementary Table II), showing that the Au/AlO_x bilayer does not behave as an efficient spin sink.

Supplementary Note 8: Relation between PHT and AMR

Both PHT and AMR arise from the planar Hall current in the FM layer, and thus PHT is expected to increase with increasing AMR. Since AMR in our NM/FM systems strongly depends on temperature, we can test the relation between PHT and AMR by measuring temperature dependence of the PHT critical current density and AMR.

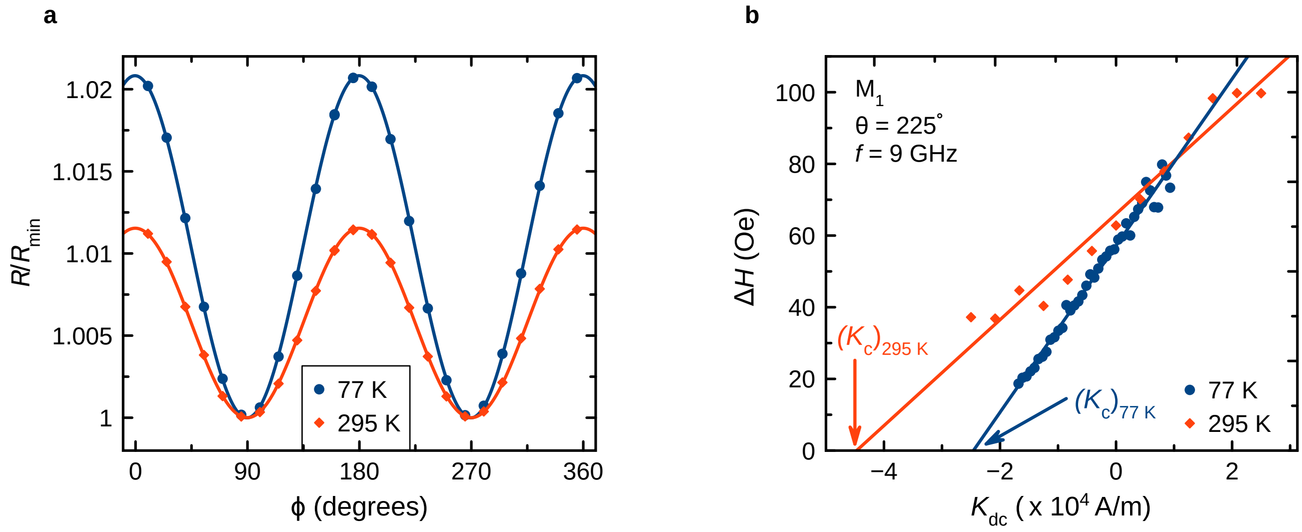

Supplementary Figure 7: **Temperature dependent measurements.** **a**, Normalized resistance of the Ta(3 nm)/Au(3.9 nm)/FM/Ta(4 nm) film as a function of 4 kOe magnetic field angle applied in the xy plane at 77 K (blue symbols) and 295 K (red symbols). **b**, ST-FMR linewidth of the M_1 mode as a function of direct sheet current density K_{dc} applied to the Ta(3 nm)/Au(3.9 nm)/FM/Ta(4 nm) nanowire device at $T = 77$ K (blue symbols) and $T = 295$ K (red symbols).

The angular dependence of normalized resistance of a Ta(3 nm)/Au(3.9 nm)/FM/Ta(4 nm) multilayer as a function of the direction of a 4 kOe saturating magnetic field applied in the plane of the sample is shown in Supplementary Fig. 7a. The data reveal that the AMR ratio $\Delta R_{\mathrm{AMR}}/R_{\mathrm{min}}$ of the multilayer increases by 80% at $T = 77$ K compared to its room temperature value: $(\Delta R_{\mathrm{AMR}}/R_{\mathrm{min}})_{295\,\mathrm{K}} = 0.0116$; $(\Delta R_{\mathrm{AMR}}/R_{\mathrm{min}})_{77\,\mathrm{K}} = 0.0209$:

$$\frac{(\Delta R_{\mathrm{AMR}}/R_{\mathrm{min}})_{77\,\mathrm{K}}}{(\Delta R_{\mathrm{AMR}}/R_{\mathrm{min}})_{295\,\mathrm{K}}} = 1.8. \tag{S7}$$

This equation gives a rough estimate of the temperature dependence of the normal component of the planar Hall current density J^z_{PHE} flowing between the FM and NM layers. This estimate, however, ignores temperature-dependent redistribution of electric current between the NM and FM layers arising from the different temperature dependences of the layer's conductivities. A more rigorous calculation of the temperature dependence of J^z_{PHE} can be done using temperature dependence of the sheet resistances reported in Supplementary Table I. According to Eq. (1) of the main text, the maximum value of J^z_{PHE} (achieved for magnetization in the xz plane making a 45° angle with the sample normal) is:

$$J^z_{\mathrm{PHE}} = \frac{1}{2}\Delta\sigma_{\mathrm{AMR}}E \approx \frac{1}{2}\frac{\Delta\rho_{\mathrm{AMR}}}{\rho_{\mathrm{FM}}}J_{\mathrm{FM}}, \tag{S8}$$

where ρ_{FM} is resistivity of the FM layer, $\Delta\rho_{\mathrm{AMR}}$ is anisotropic part of the FM layer resistivity and J_{FM} is the electric current density in the FM layer. Treating the FM and the NM layers as parallel resistors, we obtain the following expression for J_{FM}:

$$J_{\mathrm{FM}} = \frac{\rho_{\mathrm{NM}}}{\rho_{\mathrm{NM}}d_{\mathrm{FM}} + \rho_{\mathrm{FM}}d_{\mathrm{NM}}}K_{\mathrm{dc}}, \tag{S9}$$

where ρ_{NM} is resistivity of the NM layer, d_{FM} is the thickness of the FM layer, d_{NM} is the thickness of the NM layer and K_{dc} is the electrical sheet current density applied to the nanowire. Using the data in Supplementary Fig. 7a, the data in Supplementary Table I and the parallel resistor model, we obtain: $(\Delta\rho_{\mathrm{AMR}}/\rho_{\mathrm{FM}})_{295\,\mathrm{K}}$ =0.045 and $(\Delta\rho_{\mathrm{AMR}}/\rho_{\mathrm{FM}})_{77\,\mathrm{K}}$ =0.061. From Eq. (S8) and Eq. (S9), we derive an expression describing temperature dependence of J^z_{PHE} under a constant current bias I_{dc} applied to the nanowire:

$$\frac{(J^z_{\mathrm{PHE}})_{77\,\mathrm{K}}}{(J^z_{\mathrm{PHE}})_{295\,\mathrm{K}}} = \left(\frac{\Delta\rho_{\mathrm{AMR}}}{\rho_{\mathrm{FM}}}\frac{\rho_{\mathrm{NM}}}{\rho_{\mathrm{NM}}d_{\mathrm{FM}} + \rho_{\mathrm{FM}}d_{\mathrm{NM}}}\right)_{77\,\mathrm{K}} \Bigg/ \left(\frac{\Delta\rho_{\mathrm{AMR}}}{\rho_{\mathrm{FM}}}\frac{\rho_{\mathrm{NM}}}{\rho_{\mathrm{NM}}d_{\mathrm{FM}} + \rho_{\mathrm{FM}}d_{\mathrm{NM}}}\right)_{295\,\mathrm{K}} = 1.8. \tag{S10}$$

Eq. (S10) shows that the normal component of the planar Hall current density increases by a factor of 1.8 when the Ta(3 nm)/Au(3.9 nm)/FM/Ta(4 nm) nanowire is cooled from 295 K to 77 K. For this sample, the temperature dependence of J^z_{PHE} given by Eq. (S10) is the same as that obtained from the rough estimate based on temperature dependence of the multilayer AMR given by Eq. (S7).

Supplementary Fig. 7b shows the critical sheet current density for the onset of auto-oscillations K_c measured by ST-FMR in the Ta(3 nm)/Au(3.9 nm)/FM/Ta(4 nm) nanowire device at $T = 295\,\mathrm{K}$ and $T = 77\,\mathrm{K}$. This K_c measured at 9 GHz decreases from $(K_c)_{295\,\mathrm{K}} = -4.4 \times 10^4$ A/m at room temperature to $(K_c)_{77\,\mathrm{K}} = -2.5 \times 10^4$ A/m at 77 K. The value of $(K_c)_{77\,\mathrm{K}}$ measured by ST-FMR (at 9 GHz corresponding to $H = 2.83\,\mathrm{kOe}$) is in agreement with the value of K_c obtained from the microwave emission measurements at this magnetic field value, as shown in Supplementary Fig. 3b. The observed temperature-induced variation of K_c is consistent with the expected increase of the PHT efficiency due to the low-temperature increase of the planar Hall current and AMR.

Indeed, assuming the PHT origin of the antidamping torque and negligible spin polarization of the backflow current from the NM to the FM layer J^z_{BF}, the critical sheet current density can be written as:

$$K_c = C\frac{\alpha}{J^z_{\mathrm{PHE}}}, \tag{S11}$$

where α is the Gilbert damping constant of the FM layer and C is a function of the FM saturation magnetization M_s, the FM gyromagnetic ratio γ, the FM layer thickness d_{FM} and FMR frequency of the FM [18]. Since γ is nearly temperature independent and M_s for the [Co/Ni] superlattice was shown to change by less than 4% between 295 K and 4 K [4, 48, 49], we can approximate C by a temperature-independent constant.

Eq. (S11) allows to calculate temperature dependence of K_c:

$$\frac{(K_c)_{295\,\mathrm{K}}}{(K_c)_{77\,\mathrm{K}}} = \frac{(J^z_{\mathrm{PHE}})_{77\,\mathrm{K}}}{(J^z_{\mathrm{PHE}})_{295\,\mathrm{K}}}\frac{(\alpha)_{295\,\mathrm{K}}}{(\alpha)_{77\,\mathrm{K}}}. \tag{S12}$$

We employ broadband ferromagnetic resonance to measure the Gilbert damping parameter α at $T = 295\,\mathrm{K}$ and $T = 77\,\mathrm{K}$ and find $(\alpha)_{295\,\mathrm{K}} = 20.9 \times 10^{-3}$ while $(\alpha)_{77\,\mathrm{K}} = 22.2 \times 10^{-3}$. Substituting the measured values of α into Eq. (S12) and using Eq. (S10), we estimate the temperature dependence of the critical current expected from the PHT mechanism:

$$\frac{(K_c)_{295\,\mathrm{K}}}{(K_c)_{77\,\mathrm{K}}} = 1.8 \pm 0.1. \tag{S13}$$

This ratio of the critical currents measured at 295 K and 77 K is in excellent agreement with the experimentally measured ratio of 1.8, which supports the planar Hall origin of of the measured biaxial antidamping SOT.

Supplementary Note 9: Comparison of PHT and SHT efficiencies

A further test of the planar Hall origin of the observed biaxial antidamping SOT can be done via comparison of the efficiency of this SOT to the known efficiency of SHT in the same sample. We chose a Ta(3 nm)/Pt(7 nm)/FM/Ta(4 nm) nanowire for this purpose because the efficiency of SHT arising from Pt is well documented in the literature. According to Eq. (S8), the maximum efficiency of PHT (achieved for magnetization in the xz plane making a 45° angle with the sample normal, $x = z$) is given by $\frac{1}{2}\frac{\Delta\rho_{\mathrm{AMR}}}{\rho_{\mathrm{FM}}}J_{\mathrm{FM}}$. The maximum efficiency of SHT (achieved for magnetization parallel to the y axis) is given by $\theta_{\mathrm{SH}}J_{\mathrm{NM}}$, where θ_{SH} is the spin Hall angle in the NM layer. In our experiment, the efficiencies of the antidamping PHT and SHT are quantified via current-induced variation of ST-FMR linewidth $d\Delta H/dK_{\mathrm{dc}}$. Therefore, the expected ratio of $d\Delta H/dK_{\mathrm{dc}}$ measured along the $x = z$ axis and the y axis is:

$$\frac{(d\Delta H/dK_{\mathrm{dc}})_{x=z}}{(d\Delta H/dK_{\mathrm{dc}})_y} = \frac{1}{2}\frac{\Delta\rho_{\mathrm{AMR}}}{\rho_{\mathrm{FM}}\theta_{\mathrm{SH}}}\frac{J_{\mathrm{FM}}}{J_{\mathrm{NM}}}, \tag{S14}$$

Using the room-temperature sheet resistances of the NM and FM layers from Supplementary Table I and the parallel resistance model, we calculate $J_{\mathrm{FM}}/J_{\mathrm{NM}} = 0.49$ and $\Delta\rho_{\mathrm{AMR}}/\rho_{\mathrm{FM}} = 0.024$ for this sample. While the values of θ_{SH} reported in the literature vary greatly, Sagasta *et. al.* [50] have shown that θ_{SH} systematically varies with the conductivity of the Pt layer. The conductivity of the 7 nm thick Pt layer in our studies is $4.91 \times 10^4\ \mathrm{cm}^{-1}\Omega^{-1}$ at room temperature. Using Sagasta's data, we estimate the spin Hall angle $\theta_{\mathrm{SH}} = 0.035$ for our Pt layer. Substituting these values into Eq. (S14), we estimate the ratio of the PHT and SHT maximum efficiencies:

$$\frac{1}{2}\frac{\Delta\rho_{\mathrm{AMR}}}{\rho_{\mathrm{FM}}\theta_{\mathrm{SH}}}\frac{J_{\mathrm{FM}}}{J_{\mathrm{NM}}} = 0.17 \pm 0.04. \tag{S15}$$

Using the data in Fig. 3(e) and Fig. 3(f) of the main text, we calculate the experimentally measured ratio of the antidamping spin torque efficiencies:

$$\frac{(d\Delta H/dK_{\rm dc})_{x=z}}{(d\Delta H/dK_{\rm dc})_{y}} = 0.20 \pm 0.02. \tag{S16}$$

Comparison of Eq. (S15) and Eq. (S16) demonstrates that the planar Hall mechanism predicts the biaxial antidamping SOT magnitude consistent with the measured value. We note that the AMR ratio in this device is lower than in the Ta/Au/FM/Ta sample; however, it has been shown that the AMR in FMs can be significantly affected by the underlayers [51, 52]. We also note that the slightly reduced AMR in the Ta/Pt/FM/Ta wire to that of the Ta/Au/FM/Ta wire is consistent with the slightly reduced PHT effect in these respective devices, as shown in main text Fig. 3b.

The analysis in this Supplementary Note relies on the assumption that both STH and PHT are proportional to the net spin current flowing across the FM/NM interface independent on the particular mechanism responsible for the conversion of spin current into antidamping spin torque. This assumption is a good approximation when relaxation of spin angular momentum within the magnon system of the FM is much faster than relaxation of the angular momentum from magnons to the lattice [53].

Supplementary References

[1] Arora, M. *et al.* Magnetic properties of Co/Ni multilayer structures for use in STT-RAM. *J. Phys. D. Appl. Phys.* **50**, 505003 (2017).

[2] McGuire, T. & Potter, R. Anisotropic magnetoresistance in ferromagnetic 3d alloys. *IEEE Trans. Magn.* **11**, 1018–1038 (1975).

[3] Daalderop, G. H. O., Kelly, P. J. & den Broeder, F. J. A. Prediction and confirmation of perpendicular magnetic anisotropy in Co/Ni multilayers. *Phys. Rev. Lett.* **68**, 682–685 (1992).

[4] Arora, M., Hübner, R., Suess, D., Heinrich, B. & Girt, E. Origin of perpendicular magnetic anisotropy in Co/Ni multilayers. *Phys. Rev. B* **96**, 024401 (2017).

[5] Beauvillain, P. *et al.* Effect of submonolayer coverage on magnetic anisotropy of ultrathin cobalt films M/Co/Au(111) with M=Au, Cu, Pd. *J. Appl. Phys.* **76**, 6078–6080 (1994).

[6] Joly, L., Bismaths, L. T., Scheurer, F. & Weber, W. Quantum-well state induced oscillations of the electron-spin motion in Au films on Co(001). *Phys. Rev. B* **76**, 104415 (2007).

[7] Miccoli, I., Edler, F., Pfnür, H. & Tegenkamp, C. The 100th anniversary of the four-point probe technique: the role of probe geometries in isotropic and anisotropic systems. *J. Phys. Condens. Matter* **27**, 223201 (2015).

[8] Thorsteinsson, S. *et al.* Accurate microfour-point probe sheet resistance measurements on small samples. *Rev. Sci. Instrum.* **80**, 053902 (2009).

[9] Montoya, E. *et al.* Spin transport in tantalum studied using magnetic single and double layers. *Phys. Rev. B* **94**, 054416 (2016).

[10] Tulapurkar, A. A. *et al.* Spin-torque diode effect in magnetic tunnel junctions. *Nature* **438**, 339–342 (2005).

[11] Sankey, J. C. *et al.* Spin-transfer-driven ferromagnetic resonance of individual nanomagnets. *Phys. Rev. Lett.* **96**, 227601 (2006).

[12] Harder, M., Gui, Y. & Hu, C.-M. Electrical detection of magnetization dynamics via spin rectification effects. *Phys. Rep.* **661**, 1–59 (2016).

[13] Chiba, T., Schreier, M., Bauer, G. E. W. & Takahashi, S. Current-induced spin torque resonance of magnetic insulators affected by field-like spin-orbit torques and out-of-plane magnetizations. *J. Appl. Phys.* **117**, 17C715 (2015).

[14] Ando, K. *et al.* Electric detection of spin wave resonance using inverse spin-Hall effect. *Appl. Phys. Lett.* **94**, 262505 (2009).

[15] Gonçalves, A. M. *et al.* Spin torque ferromagnetic resonance with magnetic field modulation. *Appl. Phys. Lett.* **103**, 172406 (2013).

[16] Pozar, D. M. The Terminated Lossless Transmission Line. In *Microwave Engineering*, chap. 2.3, 57–60 (Wiley, 2005), 3rd edn.

[17] Slavin, A. & Tiberkevich, V. Nonlinear auto-oscillator theory of microwave generation by spin-polarized current. *IEEE Trans. Magn.* **45**, 1875–1918 (2009).

[18] Ralph, D. & Stiles, M. Spin transfer torques. *J. Magn. Magn. Mater.* **320**, 1190–1216 (2008).

[19] Duan, Z. *et al.* Nanowire spin torque oscillator driven by spin orbit torques. *Nat. Commun.* **5**, 5616 (2014).

[20] Manchon, A., Koo, H. C., Nitta, J., Frolov, S. M. & Duine, R. A. New perspectives for Rashba spin-orbit coupling. *Nat. Mater.* **14**, 871–882 (2015).

[21] Haney, P. M., Lee, H.-W., Lee, K.-J., Manchon, A. & Stiles, M. D. Current-induced torques and interfacial spin-orbit coupling. *Phys. Rev. B* **88**, 214417 (2013).

[22] Haney, P. M., Lee, H.-W., Lee, K.-J., Manchon, A. & Stiles, M. D. Current induced torques and interfacial spin-orbit coupling: Semiclassical modeling. *Phys. Rev. B* **87**, 174411 (2013).

[23] Garello, K. *et al.* Symmetry and magnitude of spinorbit torques in ferromagnetic heterostructures. *Nat. Nanotechnol.* **8**, 587–593 (2013).
[24] Kurebayashi, H. *et al.* An antidamping spinorbit torque originating from the Berry curvature. *Nat. Nanotechnol.* **9**, 211–217 (2014).
[25] Lee, K.-S. *et al.* Angular dependence of spin-orbit spin-transfer torques. *Phys. Rev. B* **91**, 144401 (2015).
[26] Ortiz Pauyac, C., Wang, X., Chshiev, M. & Manchon, A. Angular dependence and symmetry of Rashba spin torque in ferromagnetic heterostructures. *Appl. Phys. Lett.* **102**, 252403 (2013).
[27] Serpico, C., Mayergoyz, I., Bertotti, G., d'Aquino, M. & Bonin, R. Generalized Landau-Lifshitz-Gilbert equation for uniformly magnetized bodies. *Phys. B Condens. Matter* **403**, 282–285 (2008).
[28] Miron, I. M. *et al.* Current-driven spin torque induced by the Rashba effect in a ferromagnetic metal layer. *Nat. Mater.* **9**, 230–234 (2010).
[29] Park, J.-H., Kim, C. H., Lee, H.-W. & Han, J. H. Orbital chirality and Rashba interaction in magnetic bands. *Phys. Rev. B* **87**, 041301 (2013). 1207.0089.
[30] Jamali, M. *et al.* Spin-orbit torques in Co/Pd multilayer nanowires. *Phys. Rev. Lett.* **111**, 246602 (2013).
[31] Ast, C. R. *et al.* Giant spin splitting through surface alloying. *Phys. Rev. Lett.* **98**, 186807 (2007).
[32] Amin, V. P. & Stiles, M. D. Spin transport at interfaces with spin-orbit coupling: Phenomenology. *Phys. Rev. B* **94**, 104420 (2016).
[33] Montoya, E., McKinnon, T., Zamani, A., Girt, E. & Heinrich, B. Broadband ferromagnetic resonance system and methods for ultrathin magnetic films. *J. Magn. Magn. Mater.* **356**, 12–20 (2014).
[34] Montoya, E. *et al.* Magnetization Dynamics. In Camley, R. E., Celinski, Z. & Stamps, R. L. (eds.) *Magn. Surfaces, Interfaces, Nanoscale Mater.*, vol. 5, chap. 3, 113–167 (Elsevier B.V., 2015), 1 edn.
[35] Heinrich, B. & Cochran, J. Ultrathin metallic magnetic films: magnetic anisotropies and exchange interactions. *Adv. Phys.* **42**, 523–639 (1993).
[36] McMichael, R. D., Twisselmann, D. J. & Kunz, A. Localized ferromagnetic resonance in inhomogeneous thin films. *Phys. Rev. Lett.* **90**, 227601 (2003).
[37] Heinrich, B. Spin relaxation in magnetic metallic layers and multilayers. In Bland, J. A. C. & Heinrich, B. (eds.) *Ultrathin Magn. Struct.*, vol. III, chap. 5, 143–206 (Springer-Verlag, Berlin/Heidelberg, 2005).
[38] Urban, R., Woltersdorf, G. & Heinrich, B. Gilbert Damping in Single and Multilayer Ultrathin Films: Role of Interfaces in Nonlocal Spin Dynamics. *Phys. Rev. Lett.* **87**, 217204 (2001).
[39] Šimánek, E. & Heinrich, B. Gilbert damping in magnetic multilayers. *Phys. Rev. B* **67**, 144418 (2003).
[40] Tserkovnyak, Y., Brataas, A., Bauer, G. E. W. & Halperin, B. I. Nonlocal magnetization dynamics in ferromagnetic heterostructures. *Rev. Mod. Phys.* **77**, 1375–1421 (2005).
[41] Mizukami, S., Ando, Y. & Miyazaki, T. Ferromagnetic resonance linewidth for NM/80NiFe/NM films (NM=Cu, Ta, Pd and Pt). *J. Magn. Magn. Mater.* **226-230**, 1640–1642 (2001).
[42] Foros, J., Woltersdorf, G., Heinrich, B. & Brataas, A. Scattering of spin current injected in Pd(001). *J. Appl. Phys.* **97**, 10A714 (2005).
[43] Sun, Y. *et al.* Damping in yttrium iron garnet nanoscale films capped by platinum. *Phys. Rev. Lett.* **111**, 106601 (2013).
[44] Boone, C. T., Shaw, J. M., Nembach, H. T. & Silva, T. J. Spin-scattering rates in metallic thin films measured by ferromagnetic resonance damping enhanced by spin-pumping. *J. Appl. Phys.* **117**, 223910 (2015).
[45] Hahn, C. *et al.* Comparative measurements of inverse spin Hall effects and magnetoresistance in YIG/Pt and YIG/Ta. *Phys. Rev. B* **87**, 174417 (2013).
[46] Liu, L. *et al.* Spin-torque switching with the giant spin Hall effect of tantalum. *Science* **336**, 555–558 (2012).
[47] Singh, B. B., Jena, S. K. & Bedanta, S. Study of spin pumping in Co thin film vis-à-vis seed and capping layers using ferromagnetic resonance spectroscopy. *J. Phys. D. Appl. Phys.* **50**, 345001 (2017).
[48] Kurt, H., Venkatesan, M. & Coey, J. M. D. Enhanced perpendicular magnetic anisotropy in Co/Ni multilayers with a thin seed layer. *J. Appl. Phys.* **108**, 073916 (2010).
[49] Zhang, P., Xie, K., Lin, W., Wu, D. & Sang, H. Anomalous Hall effect in Co/Ni multilayers with perpendicular magnetic anisotropy. *Appl. Phys. Lett.* **104**, 082404 (2014).
[50] Sagasta, E. *et al.* Tuning the spin Hall effect of Pt from the moderately dirty to the superclean regime. *Phys. Rev. B* **94**, 060412 (2016).
[51] Li, J. X. *et al.* Pt-enhanced anisotropic magnetoresistance in Pt/Fe bilayers. *Phys. Rev. B* **90**, 214415 (2014).
[52] Rizal, C., Moa, B., Wingert, J. & Shpyrko, O. G. Magnetic Anisotropy and Magnetoresistance Properties of Co/Au Multilayers. *IEEE Trans. Magn.* **51**, 1–6 (2015).
[53] Bender, S. A. & Tserkovnyak, Y. Thermally driven spin torques in layered magnetic insulators. *Phys. Rev. B* **93**, 064418 (2016).